Measurement Report: Size-resolved secondary organic aerosol formation modulated by aerosol water uptake in wintertime haze

Jing Duan[1], Ru-Jin Huang[1,2], Ying Wang[1], Wei Xu[3], Haobin Zhong[4], Chunshui Lin[1], Wei Huang[1], Yifang Gu[1], Jurgita Ovadnevaite[5], Darius Ceburnis[5], Colin O'Dowd[5]

[1]State Key Laboratory of Loess and Quaternary Geology (SKLLQG), Center for Excellence in Quaternary Science and Global Change, Institute of Earth Environment, Chinese Academy of Sciences, Xi'an 710061, China

[2]University of Chinese Academy of Sciences, Beijing 100049, China

[3]Center for Excellence in Regional Atmospheric Environment, Institute of Urban Environment, Chinese Academy of Sciences, Xiamen, China

[4]School of Advanced Materials Engineering, Jiaxing Nanhu University, Jiaxing, 314001, China

[5]School of Physics and Centre for Climate and Air Pollution Studies, Ryan Institute, University of Galway, University Road, Galway, H91CF50, Ireland

Correspondence: Ru-Jin Huang (rujin.huang@ieecas.cn)

Abstract

This study investigated the potential effects of inorganics changes on aerosol water uptake and thus secondary organic aerosol (SOA) formation in wintertime haze, based on the size-resolved measurements of non-refractory fine particulate matter (NR-PM$_{2.5}$) in Xi'an, Northwest China. The composition of inorganic aerosol showed significant changes in winter 2018-2019 compared to winter 2013-2014, shifting from a sulfate-rich to a nitrate-rich profile. In particular, the fraction of sulfate and chloride decreased but nitrate increased in the entire size range, while ammonium mainly increased at larger particle sizes. These changes thus resulted in size-dependent evolution in water uptake. Increased water uptake was observed in most cases mainly associated with enhanced contributions of both nitrate and ammonium, with the highest increase ratio reaching 5-35% at larger particle sizes and higher relative-humidity (RH $> 70\%$). The non-negligible influence of chloride on aerosol water uptake was also emphasized. The random forest analysis coupled with a Shapley additive explanation algorithm (SHAP) further showed enhanced relative importance of aerosol water in impacting SOA formation. ~~Aerosol water contributed to the SOA formation in most cases in winter 2018-2019, and the SHAP value increased as aerosol water increased, especially at larger particle sizes.~~ Aerosol water exhibited a significant contribution to SOA formation during winter 2018-2019, particularly at larger particle sizes. The SHAP value of aerosol water increased alongside higher levels of aerosol water, indicating an enhanced contribution of aerosol water to SOA formation. This implies the majority of enhanced aerosol water uptake at larger particle sizes and high RH might facilitate the efficient aqueous-phase SOA formation. This study highlights the key role of aerosol water

as a medium to link inorganics and organics in their multiphase processes. As challenges to further improve China's air quality remain and SOA plays an increasing role in haze pollution, these results provide an insight into the size-resolved evolution characteristics and offer a guidance for future control.

1. Introduction

Particulate matter with a diameter of less than 2.5 μm ($PM_{2.5}$) has become a major concern in air pollution, which is associated with adverse health effects and regional climate change (Huang et al., 2014; Cai et al., 2017; Burnett et al., 2018; An et al., 2019; Wu et al., 2022). During the past two decades, particulate pollution in China has attracted widespread attention, and many studies have been carried out to elucidate the aerosol characteristics and formation mechanisms in haze pollution (Zhang et al., 2015; Huang et al., 2019; Zhong et al., 2020; Zheng et al., 2021; Gu et al., 2023). Aerosol characteristics such as mixing state, hygroscopicity, and acidity are strongly influenced by particle size. The size distribution of aerosol components provides essential information to elucidate the formation and transformation processes in the atmosphere, e.g., the formation and growth of new particles, or photochemical and aqueous-phase reactions (Craig et al., 2018; Kuang et al., 2020; He et al., 2021; Xu et al., 2021; Cai et al., 2022). Therefore, analyzing the characteristics of size-segregated aerosol is instrumental in comprehending their formation mechanisms in the atmosphere.

In recent years, China has implemented a series of control measures to improve air quality, including the introduction of desulfurization equipment, stricter emission standards for coal-fired power plants and industries, limitations on the number of on-road vehicles, and the replacement of coal combustion with natural gas (Fontes et al., 2017; Zheng et al., 2018; Zhang et al., 2020). As a result of these measures, the annual average concentration of $PM_{2.5}$ in China has largely decreased, and air quality has improved (Zhang et al., 2019, Wang et al., 2020; Li et al., 2021). However, further improvement of China's air quality remains a challenge and requires more studies (Xu et al., 2019; Sun et al., 2020; Wang et al., 2022). A number of recent studies have shown changes in aerosol composition and properties since the state's two-phase program to clean China's air from 2013-2020, and many studies highlight the increasing contribution of secondary aerosols and the growing role of nitrate over sulfate in haze pollution (Xu et al., 2019; Li et al., 2021; Duan et al., 2022; Zhong et al., 2022; Lin et al., 2023). This is consistent with the faster decline in SO_2 concentration than in NO_2 concentration in recent years (Chu et al., 2020). Nitrate and sulfate are two main hygroscopic substances that absorb water and provide an aqueous environment on particles, facilitating multiphase chemistry (Herrmann et al., 2015; Wu et al., 2018). For instance, condensed water enables the partitioning of water-soluble, polar organic precursors into the aqueous phase, promoting the formation of secondary organic aerosol (SOA) (Wu et al., 2018, Lv et al., 2023). The water uptake capacity of aerosols is closely related to their chemical composition, mixing state and size distribution (Liu et al.,

2019; Kim et al., 2020). The transformation of sulfate and nitrate roles in haze pollution will inevitably induce changes in aerosol water uptake capacity. However, the size-segregated changes of aerosol composition and water uptake capacity, as a consequence of air pollution control in recent years, are not well understood, and thus their impact on the SOA formation remains unclear (Xu et al., 2019; Lv et al., 2023).

In this study, we analyzed the size-resolved NR-PM$_{2.5}$ composition and OA sources in the winter 2018-2019, and compared to those in the winter 2013-2014 in Xi'an, Northwest China. Particularly, we examined the size-resolved changes in inorganic species, and discussed the size-segregated evolution of aerosol water uptake induced by the changes in inorganics. Moreover, we investigated the potential influence of aerosol water uptake changes on SOA formation processes in wintertime haze.

2. Experimental methods

2.1 Sampling and instrumentation

The campaigns in the winters of 2013-2014 and 2018-2019 were conducted at the campus of the Institute of Earth Environment, Chinese Academy of Sciences (34°23′N, 108°89′E) in downtown Xi'an, surrounded by traffic, residential, and commercial areas. Detailed descriptions of the samplings are provided in Elser et al. (2016) and Duan et al. (2022), respectively. For comparative analysis, data from December 13th, 2013 to January 6th, 2014 and from December 23rd, 2018 to January 20th, 2019 were selected for this study, considering the similar time duration and both including clean and haze periods. ~~The size-resolved NR-PM$_{2.5}$ composition was measured using an HR-ToF-AMS (Aerodyne Research Inc.) in the winter of 2013-2014, and using an SP-LToF-AMS (Aerodyne Research Inc.) in the winter of 2018-2019, respectively.~~ The size-resolved NR-PM$_{2.5}$ composition was analyzed using a high resolution-time of flight-aerosol mass spectrometer (HR-ToF-AMS, Aerodyne Research Inc.) in PToF mode during the winter of 2013-2014, and a soot particle-long time of flight-aerosol mass spectrometer (SP-LToF-AMS, Aerodyne Research Inc.) in efficient PToF (ePToF) mode in the winter of 2018-2019, respectively. In our study, the SP-LToF-AMS operated as a standard LToF-AMS in "laser off" mode, exclusively measuring non-refractory aerosols, aligning with the HR-ToF-AMS measurements. The LToF-AMS is an upgraded version of the HR-ToF-AMS, employing the same quantification principle for non-refractory organic and inorganic components while featuring an extended ToF mass spectrometer chamber to enhance mass resolution and a multiplexed chopper in ePToF mode for a higher sizing duty cycle during particle sampling. To ensure data comparability, ionization efficiency (IE) calibration and size calibration utilizing NH$_4$NO$_3$ were conducted for both instruments during the 2013-2014 and 2018-2019 campaigns, respectively. Detailed information on instrument operation and calibration can also be found in Elser et al. (2016) and Duan et al. (2022).

2.2 Data analysis

The SQUIRREL (version 1.61D) and PIKA (1.21D) software, coded in Igor Pro 6.37 (WaveMetrics), were used to analyze the size-resolved data from HR-ToF-AMS in 2013-2014 and from SP-LToF-AMS in 2018-2019. ~~Standard RIEs of 1.4, 1.1 and 1.3 were used for organics, nitrate and chloride, respectively. Experimentally determined RIEs of 1.48, and 3.37 in 2013-2014, and 1.30 and 3.70 in 2018-2019, were used for sulfate and ammonium, respectively.~~ Based on the NH_4NO_3 and $(NH_4)_2SO_4$ calibrations, experimentally determined RIEs of 1.48 and 3.37 in 2013-2014, and 1.30 and 3.70 in 2018-2019, were used for sulfate and ammonium, respectively. In comparison, default RIEs of 1.4, 1.1, and 1.3 were used for organics, nitrate, and chloride, respectively, according to previous studies (Canagaratna et al., 2007; Zhang et al., 2014; Xu et al., 2020). Additionally, incomplete detection due to particle bounce was calibrated based on the composition-dependent collection efficiency (CDCE) both in 2013-2014 and 2018-2019 (Middlebrook et al., 2012). The data and error matrices were preprocessed to obtain size-resolved NR-PM$_{2.5}$ composition (Org, SO_4^{2-}, NO_3^-, NH_4^+, and Cl^-) as well as OA mass spectra for m/z 12-120.

2.3 Size-resolved OA source apportionment

Positive matrix factorization (PMF, Paatero and Tapper, 1994) and multilinear engine (ME-2) in Igor Pro (Paatero, 1999) were used to perform the source apportionment for the size-resolved OA mass spectra. We first binned the OA mass spectra in the range of 80-2500 nm into 10 size ranges (Table S1). As the mass spectra of OA in the range of 80-113 nm and 1772-2500 nm in 2013-2014 contained many negative m/z values, we primarily performed the OA source apportionment and results discussions for the mass spectra of the remaining 8 size bins in the range of 113-1772 nm in both 2013-2014 and 2018-2019. The error matrices of size-resolved OA mass spectra were created using Eq (1) according to the methods in Ulbrich et al. (2012) and Polissar et al. (1998).

$$U_{ij}= \begin{cases} \dfrac{5}{6}LOD_i & if\ C_j \leq LOD_i \\ \sqrt{u_i^2 \times C_j^2 + LOD_i^2} & if\ C_j > LOD_i \end{cases} \qquad (1)$$

where U_{ij} refers to the uncertainty for the ith species in the jth row, and C_j refers to the measured mass loading. The three times standard deviations (3s) of the 5% lowest OA mass loading during the measurement periods were applied as the limits of detection (LOD). The relative uncertainties (u) of 20% were used for the particles, according to the transmission efficiency of the aerodynamic lens. Before PMF analysis, the ions with signal-to-noise (S/N) < 0.2 were removed and those with 0.2 < S/N < 3 were down-weighted by a factor of 2 (Xu et al., 2021).

2D matrix PMF was utilized to analyze the OA mass spectra in each size bin for both 2013-2014 and 2018-2019 campaigns. Briefly, ~~Unconstrained~~ unconstrained PMF analysis with

varied factor numbers was performed for OA mass spectra in each size bin during winter campaigns of 2013-2014 and 2018-2019. The optimal factor number was selected based on the principle that decreasing the number of factors causes mixing between different sources, and increasing the number of factors leads to factor splitting and the occurrence of non-meaningful factors. The results were evaluated by comparing the mass spectral profiles with previous studies and the correlations with tracer species. The methodology of size-resolved PMF analysis and selection of best solutions were detailed in the supplement (SI-test). As shown in Fig. S1 and S2, two Two OA sources including primary organic aerosol (POA) and SOA were resolved in each size bin in 2013-2014, and three OA sources including fossil-fuel-related OA (FFOA), biomass burning OA (BBOA) and SOA were resolved in each size bin in 2018-2019 (Fig. S1-S4). The evolution and comparison of size-resolved OA sources will be detailed in section 3.3.

2.4 Calculation of aerosol liquid water content (ALWC) and mass growth factor for inorganic aerosols (G_{mi})

The thermodynamic model ISORROPIA-II was used to calculate the ALWC. We ran the model in "reverse" mode, in which inorganic aerosol components (NH_4^+, SO_4^{2-}, NO_3^-, Cl^-) combined with ambient temperature (T) and relative humidity (RH) were input as parameters (Fountoukis and Nenes, 2007). In addition, the simulation was run in "metastable" mode and all components were assumed to be deliquescent. The thermodynamic equilibrium and phase state of those inorganic species were then simulated and the ALWC ($\mu g\,m^{-3}$) was calculated. The mass growth factor for inorganic aerosols (G_{mi}) was further calculated using the following equation:

$$G_{mi} = \frac{ALWC + m_i}{m_i} \qquad (2)$$

Where m_i is the dry mass concentration of inorganic aerosol ($\mu g\,m^{-3}$) (Song et al., 2019).

2.5 Random forest modelling

A decision tree-based random forest model was developed to understand the observed trend of SOA. We analyzed the relationship between SOA and its influencing parameters, such as RH, T, Ox (O_3+NO_2), solar radiation (SR), and aerosol liquid water. In the RF model, the whole dataset was randomly divided into a training dataset and a testing dataset. The training dataset contained 70% of the entire data, and was used to build the model. The test data contained the remaining 30% of the entire data, and was used to validate the model performance. The model's performance was evaluated based on the root mean square error (RMSE) and the correlation between predicted and observed values of the test data (R^2) (Table S2 and Fig. S9). To grow a tree, the number of independent/explanatory variables was set to 3, the minimum nod-size was set to 5, and the number of trees in the forest was set to 300, according to Grange et al. (2018) and Wang et al. (2022). Moreover, the SHapley Additive explanation (SHAP) algorithm was applied to evaluate the importance of the variables in predicting SOA, which can help produce

an interpretable model and compute the importance of variables with physical significance (Lundberg et al., 2020). Moreover, the SHapley Additive explanation (SHAP) algorithm was applied to evaluate the importance of each variable in predicting SOA. SHAP is a novel interpretable method for machine learning models based on the concept of Sharpley value in game theory, which can help interpret the complex model predictions (nonlinear fitting) and quantify the input variables' contributions to a single prediction (SOA) with physical significance (Lundberg et al., 2020). The functional expression of SHAP can be defined as follows:

$$f(x_i) = \phi_0(f,x) + \sum_{i=1}^{M} \phi_j(f,x_i) \qquad (3)$$

where $f(x_i)$ denotes the predicted value produced for each sample (x_i) with M features. $\phi_0(f, x)$ serves as the base value representing the anticipated output value of the RF model across the dataset. Additionally, $\phi_j(f, xi)$ represents the SHAP value delineating the influence of feature j in the sample (xi) on the prediction of that specific sample (Lundberg et al., 2020).

3. Results and discussion

3.1 Size-resolved changes in NR-PM$_{2.5}$ composition

The average size distribution of NR-PM$_{2.5}$ composition in winter Xi'an, as well as the relative changes between 2018-2019 and 2013-2014 are shown in Fig. 1. The peak diameter of total NR-PM$_{2.5}$ in 2018-2019 (631-890 nm) was smaller than that in 2013-2014 (890-1256 nm). The mass fraction of total secondary inorganic species (SIA, including sulfate, nitrate, and ammonium) in total NR-PM$_{2.5}$ increased from 28% to 58% as the particle size increased from 112 nm to 1772 nm in 2013-2014. Specifically, the mass fraction of sulfate displayed the largest increase from 8% to 33%, followed by nitrate from 8% to 15%, while ammonium maintained a relatively stable contribution of 10% across the entire size range. In contrast, in 2018-2019 the mass fraction of SIA in total NR-PM$_{2.5}$ increased from 25% to 51% as the particle size increased from 112 nm to 1772 nm. Unlike in 2013-2014, the mass fraction of nitrate showed the most significant contribution from 12% to 25%, followed by sulfate from 6% to 16%, and ammonium from 8% to 11% in 2018-2019.

The mass concentrations of all NR-PM$_{2.5}$ species decreased significantly in 2018-2019 compared to 2013-2014 for the entire size range, and the reduction ratio decreased as particle size increased from 112 nm to 1772 nm (Fig. 1e). However, the contribution of each species showed different variations in 2018-2019 compared to 2013-2014. In particular, the contributions of sulfate and chloride decreased obviously for the entire size range, with the reduction ratio varying from 27% to 50% for sulfate and from 68% to 39% for chloride. The significant reduction in chloride contribution, particularly in smaller particle sizes, indicates a decrease in primary chloride emission sources during winter from 2013-2014 to 2018-2019. In

contrast, the contribution of nitrate increased significantly for the entire size range, and the increase ratios at particle sizes > 317 nm (51-61%) were higher than those at particle sizes < 317 nm (31-55%). Additionally, the fraction of ammonium decreased at particle sizes < 317 nm, but increased slightly at particle sizes > 317 nm. The contribution of organics increased slightly at particle sizes < 317 nm or > 890 nm, while showed no significant change in the size range of 317-890 nm. These variations indicate the obvious changes in NR-PM$_{2.5}$ composition in winter Xi'an, which transfers from a sulfate-rich to a nitrate-rich composition with size-resolved characteristics.
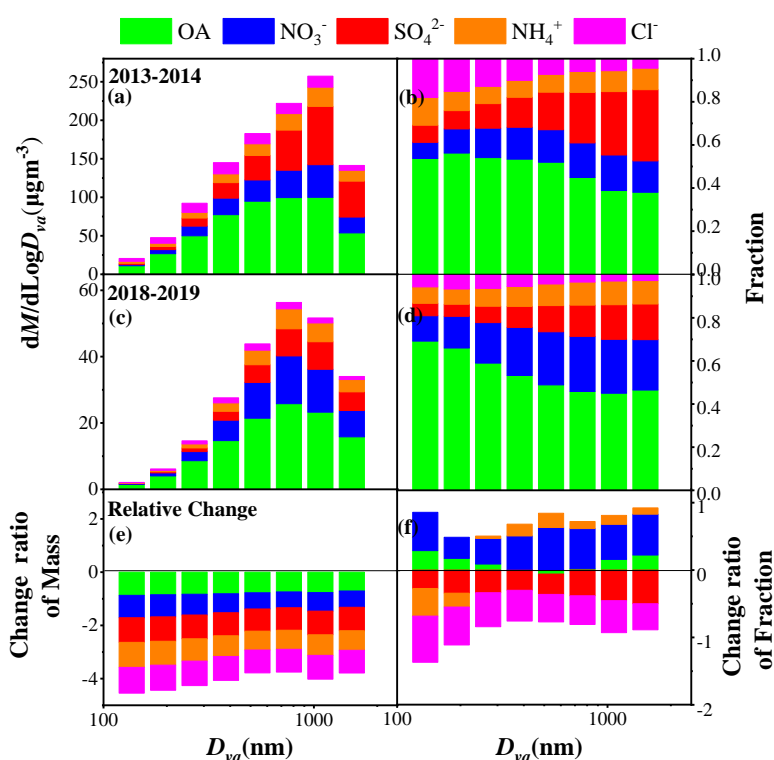
Figure 1. Average size distributions of mass concentrations and fractions of NR-PM$_{2.5}$ species (OA, NO$_3^-$, SO$_4^{2-}$, NH$_4^+$ and Cl$^-$) in winter 2013-2014 (a, b) and winter 2018-2019 (c, d) in Xi'an, as well as the relative change ratios of mass and fraction in 2018-2019 compared to 2013-2014 (e, f).

To elucidate the effects of changes in sulfate and nitrate, we further compared the size-resolved nitrate and sulfate contributions for different NR-PM$_{2.5}$ mass concentrations between 2018-2019 and 2013-2014. As shown in Fig. 2, during winter 2013-2014, nitrate and sulfate displayed similar contributions when the NR-PM$_{2.5}$ mass concentration was lower than 200 μg m^{-3}. As NR-PM$_{2.5}$ mass concentration increased from 200 μg m^{-3} to 400-800 μg m^{-3}, the contribution of sulfate increased dramatically and maintained at a stable level, while the contribution of nitrate decreased linearly. In addition, under a constant NR-PM$_{2.5}$ mass concentration, the sulfate

contribution increased with the increase of particle size, while the decrease of nitrate contribution showed no obvious dependence on particle size. As a result, the ratio of NO_3^-/SO_4^- decreased as NR-PM$_{2.5}$ mass concentration increased, with most values lower than 1, suggesting the more important role of sulfate than nitrate in haze pollution in winter 2013-2014. In comparison, during winter 2018-2019, the contributions of both nitrate and sulfate tended to increase as NR-PM$_{2.5}$ mass concentration increased across the entire mass concentration range. The increase of sulfate contribution was also more pronounced at larger particle sizes, while the increase of nitrate contribution had no obvious dependence on particle size, similar to that in 2013-2014. The ratio of NO_3^-/SO_4^- was higher than 1 in the entire NR-PM$_{2.5}$ mass concentration range and entire particle size range, suggesting the obviously increased contribution of nitrate to haze pollution in 2018-2019. However, the ratio of NO_3^-/SO_4^- showed a slightly decreased trend as NR-PM$_{2.5}$ increased, and decreased slightly as particle size increased at a constant NR-PM$_{2.5}$ mass concentration. This implies that although nitrate showed a higher contribution than sulfate in haze pollution in 2018-2019, the formation of sulfate was more efficient than nitrate under high NR-PM$_{2.5}$ mass concentrations, especially at larger particle sizes. This is similar to a recent study by Xie et al. (2023) where lower NO_3^-/SO_4^- ratio was observed in serious pollution than in moderate pollution in Hohhot, China.
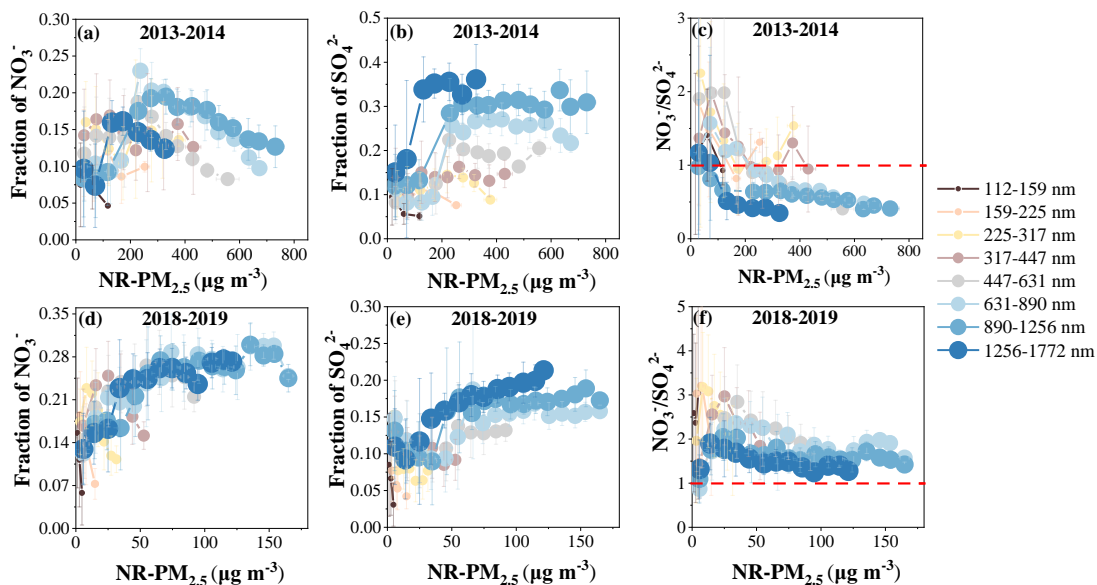
Figure 2. Variations of the fractions of nitrate and sulfate, as well as the ratio of NO_3^-/SO_4^- at different NR-PM$_{2.5}$ levels in winter 2013-2014 (a, b, c) and winter 2018-2019 (d, e, f), respectively.

3.2 Size-resolved evolution of aerosol water uptake

The changes in aerosol composition especially inorganic composition also induce changes in aerosol water uptake. The size-resolved ALWC modelled by ISORROPIA II for 2018-2019 and

2013-2014 winters were compared (Fig. ~~S3~~S10). Consistent with the size distribution of NR-PM$_{2.5}$, ALWC also peaked at 631-890 nm in 2018-2019 and 890-1256 nm in 2013-2014. The ALWC in 2018-2019 was ~5-15 times lower than that in 2013-2014 across the entire size range, due to the ~4-11 times lower inorganic mass concentrations in 2018-2019. In addition, the frequency of RH > 60% in 2018-2019 (49%) was lower than that in 2013-2014 (64%) (Fig. ~~S4~~S11). The less frequent occurrence of high RH together with the much lower inorganic mass concentration in 2018-2019 resulted in a lower ALWC than that in 2013-2014.

The mass growth factor of inorganic aerosol (G$_{mi}$), affected primarily by mass fractions of inorganic species rather than absolute mass, was further used to evaluate the response of aerosol water uptake to the changes in inorganic composition. As shown in Fig. 3, G$_{mi}$ showed an exponential increase with RH across the entire size range both in 2018-2019 and 2013-2014. The relatively size-dependent and RH-dependent changes of G$_{mi}$ in 2018-2019, compared to 2013-2014, was further analyzed (Fig. 3b). G$_{mi}$ in 2018-2019 increased relative to 2013-2014 in most cases, especially at larger particle sizes and higher RH conditions, with the highest increase ratio reaching 5-35% for particles > 317 nm at RH > 90%. However, decreased G$_{mi}$ in 2018-2019 relative to 2013-2014 was also occurred in some cases, in particular at small particle sizes and lower RH conditions. The variable changes in G$_{mi}$ were further suggested to be associated with the complicated changes in inorganic composition between 2018-2019 and 2013-2014 (Fig. ~~S5~~S12 and ~~S6~~S13).
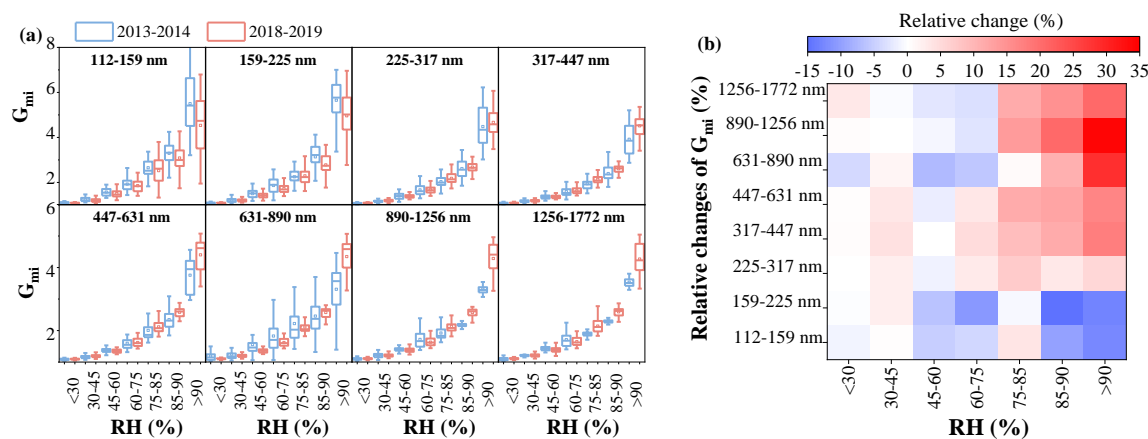
Figure 3. Variations of G$_{mi}$ as functions of RH under different size ranges between winter 2013-2014 and winter 2018-2019 in Xi'an (a), and relative changes of G$_{mi}$ in winter 2018-2019 compared to that in winter 2013-2014 across different particle sizes and different RH ranges (b).

At small particle sizes such as 112-225 nm, sulfate and nitrate in total contributed a lower mass fraction (~40-45%) to inorganics in 2013-2014, in which the sulfate and nitrate could be fully

neutralized by ammonium, and a large excessed ammonium was further combined with chloride. The important contribution of ammonium chloride to water uptake and its much higher hygroscopicity than other ones led to higher G_{mi} in 2013-2014 at small particle sizes. This is similar to a recent observation in Delhi, India, where ammonium chloride was the largest contributor to aerosol water due to higher fraction of chloride, but lower fractions of sulfate and nitrate (Chen et al., 2022). Compared to 2013-2014, the increased sulfate and nitrate, but decreased chloride fractions in 2018-2019 led to the increased contributions of ammonium sulfate and ammonium nitrate, but decreased contribution of ammonium chloride to water uptake, which then resulted in the decreased G_{mi} in 2018-2019 at small particle sizes.

At larger particle sizes, however, sulfate and nitrate in total dominated inorganics ($>60\%$) in most cases both in 2013-2014 and 2018-2019, in which ammonium sulfate, ammonium hydrogen sulfate and ammonium nitrate should be the main water-absorbing species. Under this condition, distinctly increased contribution of ammonium nitrate to water uptake in 2018-2019 will lead to increased G_{mi}, due to the higher hygroscopicity of ammonium nitrate than ammonium sulfate (Topping et al., 2005; Petters and Kreidenweis, 2007). Again, some cases with decreased G_{mi} in 2018-2019 compared to 2013-2014 at larger particle sizes were associated with a significant reduction in sulfate and nitrate contributions in 2013-2014, that is, the increased contribution of ammonium chloride to aerosol water (Fig. ~~S5~~S12). Further analysis shows the cases with increased G_{mi} in 2018-2019 compared to 2013-2014 were mainly related to enhanced contributions of both nitrate and ammonium (Fig. ~~S6~~S13). These results highlight the importance of ammonium and chloride in impacting water uptake, in addition to commonly recognized sulfate and nitrate.

3.3 Size-resolved changes of POA and SOA sources

We performed OA source apportionment in each size bin. Two OA sources including POA and SOA were resolved in winter 2013-2014, while three OA sources including FFOA, BBOA, and SOA were resolved in winter 2018-2019. The fewer OA factors resolved in this study than those in Elser et al. (2016) and Duan et al. (2022) were due to the lower resolution of size-resolved mass spectrometric data (unit mass resolution, UMR) used in this study compared to the bulk mass spectrometric data (high resolution, HR) used in Elser et al. (2016) and Duan et al. (2022). Here, we defined FFOA+BBOA as POA in winter 2018-2019 for better comparison (Fig. 4). As particle size increased from 112 nm to 1772 nm, the fraction of SOA in total OA increased from 27% to 40% in 2018-2019 and from 15% to 43% in 2013-2014. Both the mass concentrations of POA and SOA in 2018-2019 decreased relative to 2013-2014 across the entire size range. Specifically, the reduction ratio of POA in the smaller size mode was slightly higher than that in the larger size mode, which decreased from 85% to 65% as particle size increased from 112 nm to 1772 nm. In comparison, the reduction ratio of SOA showed no obvious dependence on the particle size, fluctuating around 70% as particle size increased from 112 nm

to 1772 nm. As a result, compared to 2013-2014, the fraction of SOA in total OA in 2018-2019 mainly increased at smaller sizes of 112-317 nm, while showed no obvious changes at larger sizes of 317-1772 nm due to the similar decrease ratio between POA and SOA concentrations.
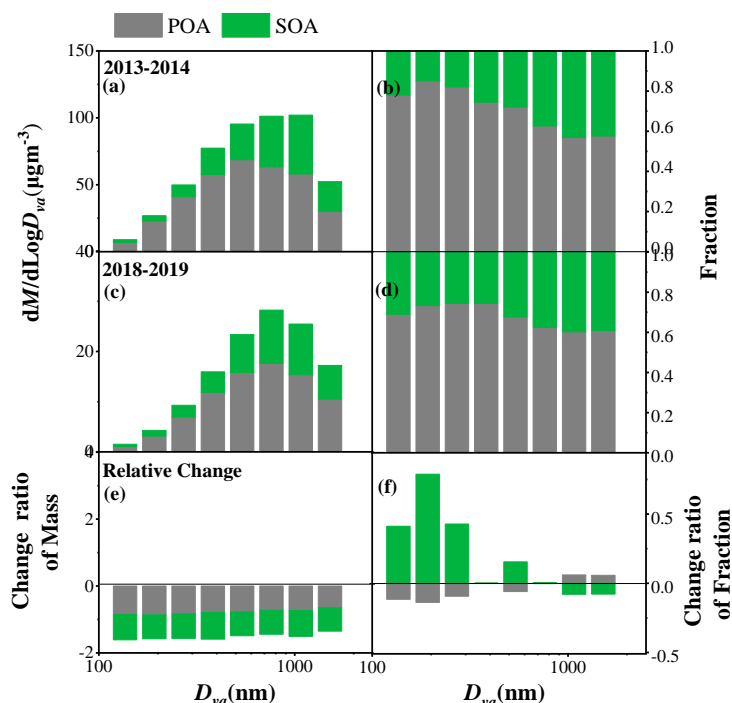
Figure 4. Average size distributions of mass concentrations and fractions of POA and SOA factors in winter 2013-2014 (a, b) and winter 2018-2019 (c, d) in Xi'an, and the relative change ratios of mass and fraction in 2018-2019, compared to 2013-2014 (e, f).

3.4 Enhanced influence of aerosol water on SOA formation

Meteorological parameters such as RH, temperature, SR, as well as Ox and aerosol water play important roles in the photochemical and aqueous-phase processes of SOA (Huang et al., 2019; Kuang et al., 2020). We used both variable importance and SHAP methods in random forest model to evaluate the size-resolved impacts of these factors in SOA formation between winter 2018-2019 and winter 2013-2014. Normalized aerosol water (ALWC/NR-PM$_{2.5}$, Liu et al., 2021) and SOA (the mass fraction of SOA in total OA) were applied to eliminate the effect of simultaneous increases or decreases in the absolute concentrations of aerosol species. Note the contribution of organics to ALWC was not considered in ISORROPIA II modelling, which will lead to an underestimation of ALWC/NR-PM$_{2.5}$. However, as the fraction of organics in total NR-PM$_{2.5}$ changed less in winter 2018-2019 compared to winter 2013-2014, particularly at particle sizes of 225-1256 nm, the effects of organic changes on ALWC/NR-PM$_{2.5}$ should also be small (Fig. 4). The performance of the model results was assessed by the correlation between the predicted and observed values of the test data (Table S2), and only those size ranges with correlation efficiency (R^2) above 0.5 in both 2013-2014 and 2018-2019 were selected for

comparison. Fig. 5 shows the relative importance of these factors in influencing SOA formation. In winter 2013-2014, the SOA formation was mainly affected by O_x and temperature, but showed a lower dependence on aerosol water with relative importance ranging from 19% to 22% across the size range of 225-1256 nm. However, enhanced impact of aerosol water on SOA formation was observed during winter 2018-2019. The relative importance of aerosol water increased from 21% to 51% as particle size increased from 225 nm to 1256 nm, and became the greatest influence factor on SOA formation for particle sizes of 447-1256 nm in winter 2018-2019.
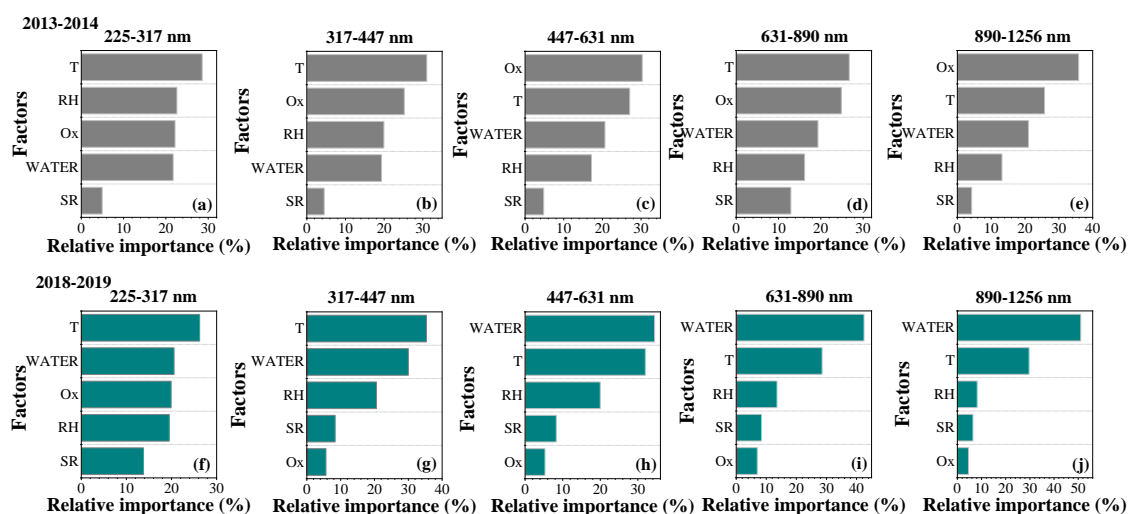
Figure 5. Random forest analysis for relative importance of factors impacting SOA formation during winter 2013-2014 (a-e) and winter 2018-2019 (f-j) in Xi'an.

Similarly, SHAP modelling results also show increased contribution of aerosol water to SOA formation in winter 2018-2019, compared to winter 2013-2014 (Fig. 6). The variables are arranged in descending order of importance from top to bottom. A negative or positive SHAP value signifies that the variable contributes more, while a SHAP value closer to zero indicates less contribution to the SOA formation. In winter 2013-2014, a positive SHAP value was observed more frequently for Ox, and the SHAP value of temperature increased positively as temperature increased across the size range of 225-1256 nm. However, aerosol water displayed an SHAP value close to zero or slightly negative in most cases. This suggests that SOA was mainly formed from photochemical oxidation in winter 2013-2014 (Elser et al., 2016). Compared to winter 2013-2014, Ox showed less contribution to SOA formation with a close to zero SHAP value more frequently in winter 2018-2019. In contrast, aerosol water contributed positively to SOA formation in most cases and the SHAP value increased as aerosol water increased, especially at larger particle sizes, suggesting enhanced positive impact of aerosol water on SOA formation in winter 2018-2019. Conversely, aerosol water exhibited

predominantly positive SHAP values across most data points, signifying a positive contribution to SOA formation in the majority of cases during the sampling period, particularly noticeable at larger particle sizes. Furthermore, the positive impact of aerosol water on SOA formation was particularly pronounced under high aerosol water conditions, with the SHAP value of aerosol water increasing as aerosol water levels intensified, implying that SOA formation may be predominantly influenced by aqueous-phase processes. These results suggest enhanced positive impact of aerosol water on SOA formation in winter 2018-2019. We suppose that the majority of enhanced aerosol water uptake in winter 2018-2019 at larger particle sizes and high RH might facilitate the efficient gas-particle partitioning of water-soluble organic compounds, and thus efficient aqueous-phase formation of SOA (Lv et al., 2023). Apart from the significant contributions of aerosol water, temperature also exhibited notable impacts on SOA formation across the size range of 225-1256 nm. The SHAP value of temperature increased with rising temperatures, indicating that higher temperatures also facilitate SOA formation in winter 2018-2019. This could be attributed to that the elevated temperatures may accelerate the chemical oxidation reactivity of precursors, thereby enhancing the processes involved in SOA formation (Jian et al., 2012; Chen et al., 2020). Additionally, a most recent study by Liu et al. (2023) revealed that urban aerosol particles could exist in a liquid state at lower RH levels with increased nitrate fraction, and the diffusion coefficient was significantly enhanced in nitrate-dominated particles, making them key seeds for secondary aerosol formation through multiphase reactions. This might be another reason for the enhanced aqueous-phase formation of SOA in winter 2018-2019, compared to winter 2013-2014 in our study. These results highlight the importance of aerosol water that links the hygroscopicity of inorganic species to multiphase processes of secondary organics, and imply the potential influence of inorganic ions on the SOA formation in urban aerosol.
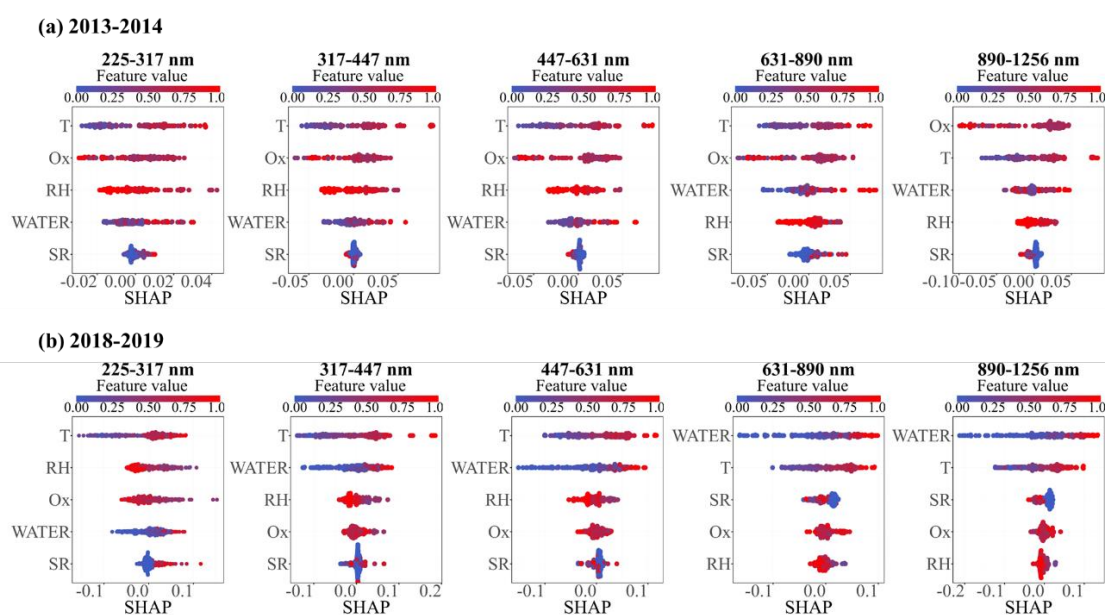
Figure 6. SHAP values for the analysis of the importance of each factor in SOA formation between winter 2013-2014 (a) and winter 2018-2019 (b) for sizes of 225-1256 nm.

4. Conclusions

Size-resolved NR-PM$_{2.5}$ composition and OA sources were compared between winters 2018-2019 and 2013-2014 in Xi'an. The NR-PM$_{2.5}$ composition changed significantly from a sulfate-rich to a nitrate-rich characteristic from winter 2013-2014 to winter 2018-2019, especially at larger particle sizes. The size-resolved changes in chemical composition resulted in size-dependent changes of aerosol water uptake. Compared to 2013-2014, G$_{mi}$ in 2018-2019 increased in most cases, especially at larger particle sizes and higher RH conditions, with the highest increase ratio reaching 5-35% for particles > 317 nm. In particular, the important role of ammonium and chloride in impacting water uptake was emphasized, in addition to sulfate and nitrate. The random forest analysis showed enhanced relative importance of aerosol water in impacting SOA formation from 2013-2014 to 2018-2019, especially at larger particle sizes. Ox and temperature showed dominant and positive contribution to SOA formation in 2013-2014, while aerosol water became the leading factor contributing positively to SOA formation in 2018-2019, implying an enhanced aqueous-phase formation of SOA. This study highlights the key role of aerosol water uptake, which links inorganic species and organic compounds in their secondary processes. The potential impact of inorganic ions, especially nitrate, in the multiphase processes of SOA and the key mechanism need to be further clarified in urban nitrate-dominant particles.

Data availability. The data used in this study are archived at the East Asian Paleoenvironmental Science Database, National Earth System Science Data Center, National Science & Technology Infrastructure of China: https://doi.org/10.12262/IEECAS.EAPSD2024001 (Duan et al., 2024).

Supplement. The Supplement related to this article is available online at

Author contributions. RJH designed the study. JD, YW, HBZ and YFG conducted the field observation. JD, RJH analyzed the data, with help from YW, WX and CSL. JD and RJH wrote the manuscript, and WH, JO, DC, and CO all commented on and discussed the manuscript.

Competing interests. The authors declare that they have no conflict of interest.

Acknowledgements. This work was supported by the National Natural Science Foundation of China (NSFC) under Grant No. 41925015, the Strategic Priority Research Program of Chinese Academy of Sciences (XDB40000000), the Key Research Program of Frontier Sciences from the Chinese Academy of Sciences (ZDBS-LY-DQC001), the Natural Science Basic Research Program of Shaanxi Province (2023-JC-QN-0319), and the National Key Research &

430   Development Program (2023YFC3705503).

Reference

An, Z. S., Huang, R.-J., Zhang, R. Y., Tie, X. X., Li, G. H., Cao, J. J., Zhou, W. J., Shi, Z. G., Han, Y. M., Gu, Z. L., and Ji, Y. M.: Severe haze in northern China: A synergy of anthropogenic emissions and atmospheric processes, Proc. Natl. Acad. Sci., 116, 8657–8666, https://doi.org/10.1073/pnas.1900125116, 2019.

Burnett, R., Chen, H., Szyszkowicz, M., Fann, N., Hubbell, B., Pope, C. A., Apte, J. S., Brauer, M., Cohen, A., Weichenthal, S., Coggins, J., Di, Q., Brunekreef, B., Frostad, J., Lim, S. S., Kan, H., Walker, K. D., Thurston, G. D., Hayes, R. B., Lim, C. C., Turner, M. C., Jerrett, M., Krewski, D., Gapstur, S. M., Diver, W. R., Ostro, B., Goldberg, D., Crouse, D. L., Martin, R. V., Peters, P., Pinault, L., Tjepkema, M., van Donkelaar, A., Villeneuve, P. J., Miller, A. B., Yin, P., Zhou, M., Wang, L., Janssen, N. A. H., Marra, M., Atkinson, R. W., Tsang, H., Quoc Thach, T., Cannon, J. B., Allen, R. T., Hart, J. E., Laden, F., Cesaroni, G., Forastiere, F., Weinmayr, G., Jaensch, A., Nagel, G., Concin, H., and Spadaro, J. V.: Global estimates of mortality associated with long-term exposure to outdoor fine particulate matter, P. Natl. Acad. Sci. USA, 115, 9592–9597, https://doi.org/10.1073/pnas.1803222115, 2018.

Cai, W., Li, K., Liao, H., Wang, H., and Wu, L.: Weather conditions conducive to Beijing severe haze more frequent under climate change, Nat. Clim. Change, 7, 257–263, https://doi.org/10.1038/nclimate3249, 2017.

Cai, M., Huang, S., Liang, B., Sun, Q., Liu, L., Yuan, B., Shao, M., Hu, W., Chen, W., Song, Q., Li, W., Peng, Y., Wang, Z., Chen, D., Tan, H., Xu, H., Li, F., Deng, X., Deng, T., Sun, J., and Zhao, J.: Measurement report: Distinct size dependence and diurnal variation in organic aerosol hygroscopicity, volatility, and cloud condensation nuclei activity at a rural site in the Pearl River Delta (PRD) region, China, Atmos. Chem. Phys., 22, 8117–8136, https://doi.org/10.5194/acp-22-8117-2022, 2022.

Canagaratna, M. R., Jayne, J. T., Jiménez, J. L., Allan, J. D., Alfarra, M. R., Zhang, Q., Onasch, T. B., Drewnick, F., Coe, H., Middlebrook, A., Delia, A., Williams, L. R., Trimborn, A. M., Northway, M. J., DeCarlo, P. F., Kolb, C. E., Davidovits, P., and Worsnop, D. R.: Chemical and Microphysical Characterization of Ambient Aerosols with the Aerodyne Aerosol Mass Spectrometer, Mass Spectrom. Rev., 26, 185–222, 2007.

Chen, Y., Wang, Y., Nenes, A., Wild, O., Song, S., Hu, D., Liu, D., He, J., Hildebrandt Ruiz, L., Apte, J. S., Gunthe, S. S., and Liu, P.: Ammonium Chloride Associated Aerosol Liquid Water Enhances Haze in Delhi, India, Environ. Sci. Technol., 56, 7163–7173, https://doi.org/10.1021/acs.est.2c00650, 2022.

Chen, Z., Chen, D., Zhao, C., Kwan, M.-p., Cai, J., Zhuang, Y., Zhao, B., Wang, X., Chen, B., Yang, J., Li, R., He, B., Gao, B., Wang, K., and Xu, B.: Influence of meteorological conditions on PM2.5 concentrations across China: A review of methodology and

mechanism, Environ. Int., 139, 105558, https://doi.org/10.1016/j.envint.2020.105558, 2020.

470   Chu, B., Ma, Q., Liu, J., Ma, J., Zhang, P., Chen, T., Feng, Q., Wang, C., Yang, N., Ma, H., Ma, J., Russell, A. G., and He, H.: Air Pollutant Correlations in China: Secondary Air Pollutant Responses to NOx and SO2 Control, Environ. Sci. Tech. Let., 7, 695 – 700, https://doi.org/10.1021/acs.estlett.0c00403, 2020.

Craig, R. L. and Ault, A. P.: Aerosol Acidity: Direct Measurement from a Spectroscopic Method,
475   in: Multiphase Environmental Chemistry in the Atmosphere, ACS Symposium Series, 1299, American Chemical Society, 171–191, https://doi.org/10.1021/bk-2018-1299.ch009, 2018.

Duan, J., Huang, R. J., Gu, Y., Lin, C., Zhong, H., Xu, W., Liu, Q., You, Y., Ovadnevaite, J., Ceburnis, D., Hoffmann, T., and O'Dowd, C.: Measurement report: Large contribution of
480   biomass burning and aqueous-phase processes to the wintertime secondary organic aerosol formation in Xi'an, Northwest China, Atmos. Chem. Phys., 22, 10139–10153, https://doi.org/10.5194/acp-22-10139-2022, 2022.

Elser, M., Huang, R. J., Wolf, R., Slowik, J. G., Wang, Q., Canonaco, F., Li, G., Bozzetti, C., Daellenbach, K. R., Huang, Y., Zhang, R., Li, Z., Cao, J., Baltensperger, U., El-Haddad, I.,
485   and André, P.: New insights into PM2.5 chemical composition and sources in two major cities in China during extreme haze events using aerosol mass spectrometry, Atmos. Chem. Phys., 16, 3207–3225, https://doi.org/10.5194/acp-16-3207-2016, 2016.

Fontes, T., Li, P. L., Barros, N., and Zhao, P. J.: Trends of PM2.5 concentrations in China: A long   term   approach,   J.   Environ.   Manage.,   196,   719–732.
490   https://doi.org/10.1016/j.jenvman.2017.03.074, 2017.

Fountoukis, C. and Nenes, A.: ISORROPIA II: a computationally efficient thermodynamic equilibrium model for $K^+–Ca^{2+}–Mg^{2+}–NH_4^+–Na^+–SO_4^{2-}–NO_3^-–Cl^-–H_2O$ aerosols, Atmos. Chem. Phys., 7, 4639–4659, 2007.

Grange, S. K., Carslaw, D. C., Lewis, A. C., Boleti, E., and Hueglin, C.: Random forest
495   meteorological normalisation models for Swiss PM10 trend analysis, Atmos. Chem. Phys., 18, 6223–6239, https://doi.org/10.5194/acp-18-6223-2018, 2018.

Gu, Y., Huang, R.-J., Duan, J., Xu, W., Lin, C., Zhong, H., Wang, Y., Ni, H., Liu, Q., Xu, R., Wang, L., and Li, Y. J.: Multiple pathways for the formation of secondary organic aerosol in the North China Plain in summer, Atmos. Chem. Phys., 23, 5419–5433,
500   https://doi.org/10.5194/acp-23-5419-2023, 2023.

He, Y., Akherati, A., Nah, T., Ng, N. L., Garofalo, L. A., Farmer, D. K., Shiraiwa, M., Zaveri, R. A., Cappa, C. D., Pierce, J. R., and Jathar, S. H.: Particle Size Distribution Dynamics Can Help Constrain the Phase State of Secondary Organic Aerosol, Environ. Sci. Technol., 55, 1466–1476, https://doi.org/10.1021/acs.est.0c05796, 2021.

505   Herrmann, H., Schaefer, T., Tilgner, A., Styler, S., Weller, C., Teich, M., and Otto, T.:

Tropospheric Aqueous-Phase Chemistry: Kinetics, Mechanisms, and Its Coupling to a Changing Gas Phase, Chem. Rev., 115, 4259–4334, https://doi.org/10.1021/cr500447k, 2015.

Huang, R.-J., Zhang, Y. L., Bozzetti, C., Ho, K.-F., Cao, J. J., Han, Y. M., Daellenbach, K. R.,
510   Slowik, J. G., Platt, S. M., Canonaco, F., Zotter, P., Wolf, R., Pieber, S. M., Bruns, E. A., Crippa, M., Ciarelli, G., Piazzalunga, A., Schwikowski, M., Abbaszade, G., Schnelle-Kreis, J., Zimmermann, R., An, Z., Szidat, S., Baltensperger, U., Haddad, I. E., and Prévôt, A. S. H.: High secondary aerosol contribution to particulate pollution during haze events in China, Nature, 514, 218–222, https://doi.org/10.1038/nature13774, 2014.

515 Huang, R.-J., Wang, Y., Cao, J., Lin, C., Duan, J., Chen, Q., Li, Y., Gu, Y., Yan, J., Xu, W., Fröhlich, R., Canonaco, F., Bozzetti, C., Ovadnevaite, J., Ceburnis, D., Canagaratna, M.R., Jayne, J., Worsnop, D.R., El-Haddad, I., Prévôt, A.S.H., and O'Dowd, C.D.: Primary emissions versus secondary formation of fine particulate matter in the most polluted city (Shijiazhuang) in North China, Atmos. Chem. Phys., 19, 2283–2298, 2019.

520 Jian, L., Zhao, Y., Zhu, Y. P., Zhang, M. B., and Bertolatti, D.: An application of arima model to predict submicron particle concentrations from meteorological factors at a busy roadside in hangzhou, China, Sci. Total Environ., 426, 336–345, 2012.

Kim, N., Yum, S. S., Park, M., Park, J. S., Shin, H. J., and Ahn, J. Y.: Hygroscopicity of urban aerosols and its link to size-resolved chemical composition during spring and summer in
525   Seoul, Korea, Atmos. Chem. Phys., 20, 11245–11262, https://doi.org/10.5194/acp-20-11245-2020, 2020.

Kuang, Y., He, Y., Xu, W. Y., Yuan, B., Zhang, G., Ma, Z. Q., Wu, C. H., Wang, C. M., Wang, S. H., Zhang, S. Y., Tao, J. C., Ma, N., Su, H., Cheng, Y. F., Shao, M., and Sun, Y. L.: Photochemical aqueous-phase reactions induce rapid daytime formation of oxygenated
530   organic aerosol on the North China Plain, Environ. Sci. Technol., 54(7), 3849–3860, https://doi.org/10.1021/acs.est.9b06836, 2020.

Li, J., Gao, W., Cao, L., Xiao, Y., Zhang, Y., Zhao, S., Liu, Z., Liu, Z., Tang, G., Ji, D., Hu, B., Song, T., He, L., Hu, M., and Wang, Y. S.: Significant changes in autumn and winter aerosol composition and sources in Beijing from 2012 to 2018: Effects of clean air actions,
535   Environ. Pollut., 268, 115855, https://doi.org/10.1016/j.envpol.2020.115855, 2021.

Lin, C., Huang, R.-J., Zhong, H., Duan, J., Wang, Z., Huang, W., and Xu, W.: Elucidating ozone and PM2.5 pollution in the Fenwei Plain reveals the co-benefits of controlling precursor gas emissions in winter haze, Atmos. Chem. Phys., 23, 3595–3607, https://doi.org/10.5194/acp-23-3595-2023, 2023.

540 Liu, Y., Wu, Z., Huang, X., Shen, H., Bai, Y., Qiao, K., Meng, X., Hu, W., Tang, M., and He, L.: Aerosol phase state and its link to chemical composition and liquid water content in a subtropical coastal megacity, Environ. Sci. Technol., 53, 5027–5033, https://doi.org/10.1021/acs.est.9b01196, 2019.

Liu, Y., Feng, Z., Zheng, F., Bao, X., Liu, P., Ge, Y., Zhao, Y., Jiang, T., Liao, Y., Zhang, Y., Fan, X., Yan, C., Chu, B., Wang, Y., Du, W., Cai, J., Bianchi, F., Petäjä, T., Mu, Y., He, H., and Kulmala, M.: Ammonium nitrate promotes sulfate formation through uptake kinetic regime, Atmos. Chem. Phys., 21, 13269–13286, https://doi.org/10.5194/acp-21-13269-2021, 2021.

Liu, Y. C., Wu, Z. J., Qiu, Y. T., Tian, P., Liu, Q., Chen, Y., Song, M., and Hu, M.: Enhanced nitrate fraction: Enabling urban aerosol particles to remain in a liquid state at reduced relative humidity, Geophys. Res. Lett., 50(21), e2023GL105505, https://doi.org/10.1029/2023GL105505, 2023.

Lundberg, S. M., Erion, G., Chen, H., DeGrave, A., Prutkin, J. M., Nair, B., Katz, R., Himmelfarb, J., Bansal, N., and Lee, S.-I.: From local explanations to global understanding with explainable AI for trees, Nat. Mach. Intell., 2, 56–67, https://doi.org/10.1038/s42256-019-0138-9, 2020.

Lv, S. J., Wu, C., Wang, F. L., Liu, X. D., Zhang, S., Chen, Y. B., Zhang, F., Yang, Y., Wang, H. L., Huang, C., Fu, Q. Y., Duan, Y. S., and Wang, G. H.: Nitrate-enhanced gas-to-particle-phase partitioning of water-soluble organic compounds in Chinese urban atmosphere: implications for secondary organic aerosol formation, Environ. Sci. Technol. Lett., 10, 14–20, https://doi.org/10.1021/acs.estlett.2c00894, 2023.

Middlebrook, A. M., Bahreini, R., Jimenez, J. L., and Canagaratna, M. R.: Evaluation of composition-dependent collection efficiencies for the Aerodyne Aerosol Mass Spectrometer using field data, Aerosol Sci. Tech., 46, 258–271, https://doi.org/10.1080/02786826.2011.620041, 2012.

Paatero, P. and Tapper, U.: Positive Matrix Factorization: A non-negative factor model with optimal utilization of error estimates of data values, Environmetrics, 5, 111–126, https://doi.org/10.1002/env.3170050203, 1994.

Paatero, P.: The multilinear engine: a table-driven, least squares program for solving multilinear problems, including the n-way parallel factor analysis model, J. Comput. Graph. Stat., 8, 854–888, https://doi.org/10.1080/10618600.1999.10474853, 1999.

Petters, M. D. and Kreidenweis, S. M.: A single parameter representation of hygroscopic growth and cloud condensation nucleus activity, Atmos. Chem. Phys., 7, 1961–1971, https://doi.org/10.5194/acp-7-1961-2007, 2007.

Polissar, A. V., Hopke, P. K., Malm, W. C., and Sisler, J. F.: Atmospheric Aerosol over Alaska: 2. Elemental Composition and Sources, J. Geophys. Res.-Atmos., 103, 19045–19057, https://doi.org/10.1029/98JD01212, 1998.

Song, S., Nenes, A., Gao, M., Zhang, Y., Liu, P., Shao, J., Ye, D., Xu, W., Lei, L., Sun, Y., Liu, B., Wang, S., and McElroy, M. B.: Thermodynamic Modeling Suggests Declines in Water Uptake and Acidity of Inorganic Aerosols in Beijing Winter Haze Events during 2014/2015–2018/2019, Environ. Sci. Technol. Lett., 752–760,

https://doi.org/10.1021/acs.estlett.9b00621, 2019.

Sun, Y., Lei, L., Zhou, W., Chen, C., He, Y., Sun, J., Li, Z., Xu, W., Wang, Q., Ji, D., Fu, P., Wang, Z., and Worsnop, D.: A chemical cocktail during the COVID-19 outbreak in Beijing, China: insights from six-year aerosol particle composition measurements during the Chinese New Year holiday, Sci. Total Environ., 742, 140739, https://doi.org/10.1016/j.scitotenv.2020.140739, 2020.

Topping, D. O., Mcfiggans, G. B., and Coe, H.: A curved multicomponent aerosol hygroscopicity model framework: Part 1– Inorganic compounds, Atmos. Chem. Phys., 5, 1205–1222, https://doi.org/10.5194/acp-5-1205-2005, 2005.

Ulbrich, I. M., Canagaratna, M. R., Cubison, M. J., Zhang, Q., Ng, N. L., Aiken, A. C., and Jimenez, J. L.: Three-dimensional factorization of size-resolved organic aerosol mass spectra from Mexico City, Atmos. Meas. Tech., 5, 195–224, https://doi.org/10.5194/amt-5-195-2012, 2012.

Wang, M., Zhang, Z., Yuan, Q., Li, X., Han, S., Lam, Y., Cui, L., Huang, Y., Cao, J., and Lee, S.-C.: Slower than expected reduction in annual PM2.5 in Xi'an revealed by machine learning-based meteorological normalization, Sci. Total Environ., 841, 156740, https://doi.org/10.1016/j.scitotenv.2022.156740, 2022.

Wang, Y. H., Gao, W. K., Wang, S. A., Song, T., Gong, Z. Y., Ji, D. S., Wang, L. L., Liu, Z. R., Tang, G. Q., Huo, Y. F., Tian, S. L., Li, J. Y., Li, M. G., Yang, Y., Chu, B. W., Petäjä, T., Kerminen, V.-M., He, H., Hao, J. M., Kulmala, M., Wang, Y. S., and Zhang, Y. H.: Contrasting trends of PM2.5 and surface-ozone concentrations in China from 2013 to 2017, Natl. Sci. Rev., 7, 1331–1339, https://doi.org/10.1093/nsr/nwaa032, 2020.

Wu, D., Zheng, H., Li, Q., Jin, L., Lyu, R., Ding, X., Huo, Y., Zhao, B., Jiang, J., and Chen, J.: Toxic potency-adjusted control of air pollution for solid fuel combustion, Nat. Energy, 7, 194–202, https://doi.org/10.1038/s41560-021-00951-1, 2022.

Wu, Z., Wang, Y., Tan, T., Zhu, Y., Li, M., Shang, D., Wang, H., Lu, K., Guo, S., Zeng, L., and Zhang, Y.: Aerosol liquid water driven by anthropogenic inorganic salts: implying its key role in haze formation over the North China Plain, Environ. Sci. Tech. Let., 5, 160–166, https://doi.org/10.1021/acs.estlett.8b00021, 2018.

Xie, F., Su, Y., Tian, Y., Shi, Y., Zhou, X., Wang, P., Yu, R., Wang, W., He, J., Xin, J., and Lü, C.: The shifting of secondary inorganic aerosol formation mechanisms during haze aggravation: the decisive role of aerosol liquid water, Atmos. Chem. Phys., 23, 2365–2378, https://doi.org/10.5194/acp-23-2365-2023, 2023.

Xu, J., Ge, X., Zhang, X., Zhao, W., Zhang, R., and Zhang, Y.: COVID-19 impact on the concentration and composition of submicron particulate matter in a typical city of Northwest China, Geophys. Res. Lett., 47, e2020GL089035, https://doi.org/10.1029/2020GL089035, 2020.

Xu, W., Sun, Y., Wang, Q., Zhao, J., Wang, J., Ge, X., Xie, C., Zhou, W., Du, W., Li, J., Fu, P.,

Wang, Z., Worsnop, D. R., and Coe, H.: Changes in aerosol chemistry from 2014 to 2016 in winter in Beijing: Insights from high-resolution aerosol mass spectrometry, J. Geophys. Res.-Atmos., 124, 1132–1147, https://doi.org/10.1029/2018JD029245, 2019.

Xu, W., Chen, C., Qiu, Y., Xie, C., Chen, Y., Ma, N., Xu, W., Fu, P., Wang, Z., Pan, X., Zhu, J., Ng, N. L., and Sun, Y.: Size-resolved characterization of organic aerosol in the North China Plain: new insights from high resolution spectral analysis, Environ. Sci. Atmos., 1, 346–358, https://doi.org/10.1039/D1EA00025J, 2021.

Zhang, Q., Zheng, Y., Tong, D., Shao, M., Wang, S., Zhang, Y., Xu, X., Wang, J., He, H., Liu, W., Ding, Y., Lei, Y., Li, J., Wang, Z., Zhang, X., Wang, Y., Cheng, J., Liu, Y., Shi, Q., Yan, L., Geng, G., Hong, C., Li, M., Liu, F., Zheng, B., Cao, J., Ding, A., Gao, J., Fu, Q., Huo, J., Liu, B., Liu, Z., Yang, F., He, K., and Hao, J.: Drivers of Improved PM2.5 Air Quality in China from 2013 to 2017, P. Natl. Acad. Sci. USA, 116, 24463–24469, https://doi.org/10.1073/pnas.1907956116, 2019.

Zhang, R. Y., Wang, G. H., Guo, S., Zarnora, M. L., Ying, Q., Lin, Y., Wang, W. G., Hu, M., and Wang, Y.: Formation of Urban Fine Particulate Matter, Chem. Rev., 115, 3803–3855, https://doi.org/10.1021/acs.chemrev.5b00067, 2015.

Zhang, J. K., Sun, Y., Liu, Z. R., Ji, D. S., Hu, B., Liu, Q., and Wang, Y. S.: Characterization of submicron aerosols during a month of serious pollution in Beijing, 2013, Atmos. Chem. Phys., 14, 2887–2903, https://doi.org/10.5194/acp-14-2887-2014, 2014.

Zhang, Y., Vu, T. V., Sun, J., He, J., Shen, X., Lin, W., Zhang, X., Zhong, J., Gao, W., Wang, Y., Fu, T. M., Ma, Y., Li, W., and Shi, Z.: Significant Changes in Chemistry of Fine Particles in Wintertime Beijing from 2007 to 2017: Impact of Clean Air Actions, Environ. Sci. Technol., 54, 1344–1352, https://doi.org/10.1021/acs.est.9b04678, 2020.

Zheng, B., Tong, D., Li, M., Liu, F., Hong, C., Geng, G., Li, H., Li, X., Peng, L., Qi, J., Yan, L., Zhang, Y., Zhao, H., Zheng, Y., He, K., and Zhang, Q.: Trends in China's anthropogenic emissions since 2010 as the consequence of clean air actions, Atmos. Chem. Phys., 18, 14095–14111, https://doi.org/10.5194/acp-18-14095-2018, 2018.

Zheng, Y., Chen, Q., Cheng, X., Mohr, C., Cai, J., Huang, W., Shrivastava, M., Ye, P., Fu, P., Shi, X., Ge, Y., Liao, K., Miao, R., Qiu, X., Koenig, T. K., and Chen, S.: Precursors and Pathways Leading to Enhanced Secondary Organic Aerosol Formation during Severe Haze Episodes, Environ. Sci. Technol., 55, 15680–15693, https://doi.org/10.1021/acs.est.1c04255, 2021.

Zhong, H., Huang, R.-J., Duan, J., Lin, C., Gu, Y., Wang, Y., Li, Y. J., Zheng, Y., Chen, Q., Chen, Y., Dai, W. T., Ni, H. Y., Cao, J. J., Worsnop, D. R., Xu, W., Ovadnevaite, J., Ceburnis, D., and O'Dowd, C. D.: Seasonal variations in the sources of organic aerosol in Xi'an, Northwest China: The importance of biomass burning and secondary formation, Sci. Total. Environ., 737, 139666, https://doi.org/10.1016/j.scitotenv.2020.139666, 2020.

Zhong, H., Huang, R.-J., Lin, C., Xu, W., Duan, J., Gu, Y., Huang, W., Ni, H., Zhu, C., You, Y.,

Wu, Y., Zhang, R., Ovadnevaite, J., Ceburnis, D., and O'Dowd, C. D.: Measurement report: On the contribution of long-distance transport to the secondary aerosol formation and aging, Atmos. Chem. Phys., 22, 9513–9524, https://doi.org/10.5194/acp-22-9513-2022, 2022.

660

Supplement of:

Measurement Report: Size-resolved secondary organic aerosol formation modulated by aerosol water uptake in wintertime haze

Jing Duan[1], Ru-Jin Huang[1,2], Ying Wang[1], Wei Xu[3], Haobin Zhong[4], Chunshui Lin[1], Wei, Huang[1], Yifang Gu[1], Jurgita Ovadnevaite[5], Darius Ceburnis[5], Colin O'Dowd[5]

[1]State Key Laboratory of Loess and Quaternary Geology (SKLLQG), Center for Excellence in Quaternary Science and Global Change, Institute of Earth Environment, Chinese Academy of Sciences, Xi'an 710061, China
[2]University of Chinese Academy of Sciences, Beijing 100049, China
[3]Center for Excellence in Regional Atmospheric Environment, Institute of Urban Environment, Chinese Academy of Sciences, Xiamen, China
[4]School of Advanced Materials Engineering, Jiaxing Nanhu University, Jiaxing, 314001, China
[5]School of Physics and Centre for Climate and Air Pollution Studies, Ryan Institute, University of Galway, University Road, Galway, H91CF50, Ireland
Correspondence: Ru-Jin Huang (rujin.huang@ieecas.cn)

SI-text: OA source apportionment

For OA mass spectra in each size bin during winter campaigns of 2013-2014 and 2018-2019, unconstrained PMF runs with varying factor numbers were conducted. The optimal solution for the size-resolved PMF was determined based on the principle that reducing the number of factors results in the mixing of different sources, while increasing the number of factors leads to factor splitting or mixing again and the emergence of non-meaningful factors.

Briefly, for the PMF results in each size bin in 2013-2014, the 2-factor solution resolved a POA source with prominent signal peaks at fragments such as m/z 55 (mainly $C_4H_7^+$), m/z 57 (mainly $C_4H_9^+$), and m/z 60 (mainly $C_2H_4O_2^+$), while a much lower signal at m/z 44 (mainly CO_2^+, a typical fragment in aging or secondary OA sources). These features align with typical characteristics of POA profiles reported in previous studies at various urban sites (Ng et al., 2010, 2011; Hu et al., 2016). In contrast, the second factor exhibited significantly lower signals for primary fragments like m/z 55, 57, and 60, but displayed a dominant signal peak at m/z 44, indicating its aging or secondary nature (Ng et al., 2011). Consequently, this factor was classified as a SOA source (Fig. S1). Upon increasing the factor number to 3, no distinct POA categories like HOA, COA, or BBOA were further resolved. However, the SOA factor was split into two factors, with signals at m/z 29 and m/z 44 divided in Factor 2, and signals at m/z 28 and m/z 43 divided in Factor 3, respectively (Fig. S5). Consequently, the 2-factor solution was selected as the best performance, and two OA sources, comprising POA and SOA, were identified in each size bin in 2013-2014.

For the PMF results in each size bin in 2018-2019, Factor 2 in the 2-factor solution was evidently a mixture of m/z 44 and numerous primary ions of m/z > 50, notably m/z 60 originating from BBOA (Fig. S6). This observation suggests that the 2-factor solution did not clearly distinguish between SOA and POA. Upon increasing the factor number to 3 (Fig. S3), two primary sources with much lower contribution from m/z 44, and one secondary source with dominant signal peaks at m/z 44 were resolved. Specifically, as a tracer ion for biomass burning sources, the signal of m/z 60 appeared primarily in Factor 2, with no significant mixing observed in Factor 1 and Factor 3. This indicates that Factor 2 represents a clean BBOA source identified through PMF analysis (Cubison et al., 2011). Factor 1, another primary source unaffected by m/z 60 interference, was characterized by prominent hydrocarbon ion series of C_nH_{2n-1} and C_nH_{2n+1}, defining it as a fossil-fuel-related OA (FFOA) according to previous studies (Sun et al., 2016, 2018). In comparison, Factor 3 exhibited a dominant signal peak at m/z 44, which was defined as a SOA source. The 4-factor solution was further analyzed to determine if increasing the number of factors could resolve more refined primary or secondary sources. As shown in Fig. S7, increasing the factor number to 4 resulted in newly generated factors frequently showing significant mixing, such as a mixture of BBOA and FFOA in the smaller size ranges and a blend of secondary and primary sources, especially m/z 60, in the larger size ranges. Moreover, continuing to increase the factor number to 5 did not alleviate the mixing issues, instead, other non-meaningful factors were observed (Fig. S8). Therefore, the 3-factor solution was selected as the best performance, and three OA sources, comprising FFOA, BBOA and SOA, were identified in each size bin in 2018-2019.

Table S1 A summary of size ranges of 10 bins in the range of 80 – 2500 nm.

Bin number	Size (nm)
Bin1	80-112
Bin2	112-159
Bin3	159-225
Bin4	225-317
Bin5	317-447
Bin6	447-631
Bin7	631-890
Bin8	890-1256
Bin9	1256-1772
Bin10	1772-2500

Table S2 Evaluation of random forest regression model.

campaign	Size (nm)	RMSE[a]	R^{2}[b]
winter 2013-2014	112-159	0.126	0.17
	159-225	0.034	0.63
	225-317	0.036	0.60
	317-447	0.049	0.73
	447-631	0.043	0.74
	631-890	0.068	0.69
	890-1256	0.052	0.67
	1256-1772	0.076	0.36
winter 2018-2019	112-159	0.196	0.09
	159-225	0.108	0.37
	225-317	0.075	0.54
	317-447	0.075	0.53
	447-631	0.066	0.61
	631-890	0.057	0.71
	890-1256	0.053	0.80
	1256-1772	0.074	0.75

[a] RMSE (Root mean square error) is the square root of the expected squared difference between the predicted and observed values.

[b]R^2 is the correlation between the observed and random forest predicted SOA%.
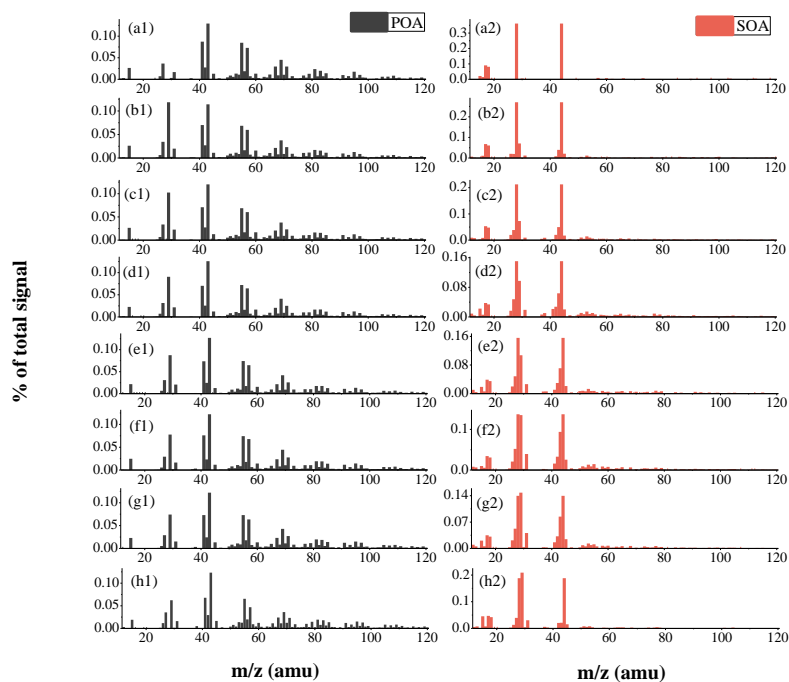
Figure S1. Mass spectra of (a1-h1) POA, (a2-h2) SOA under different size ranges of 112-159 nm, 159-225 nm, 225-317 nm, 317-447 nm, 447-631 nm, 631-890 nm, 890-1256 nm, and 1256-1772 nm, respectively, in winter 2013-2014 in Xi'an.
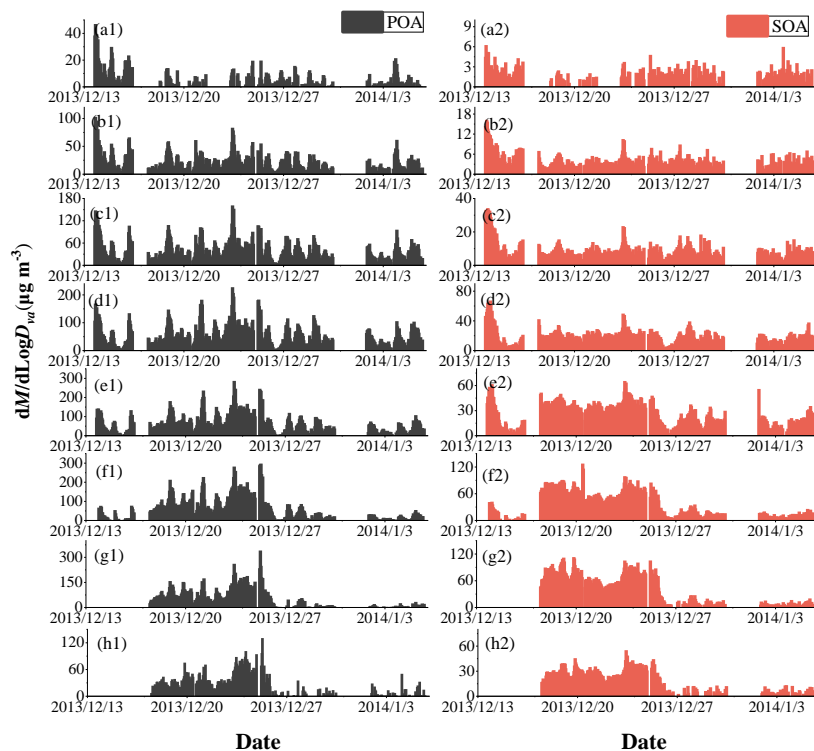
Figure S2. The time series of (a1-h1) POA, (a2-h2) SOA under different size ranges of 112-159 nm, 159-225 nm, 225-317 nm, 317-447 nm, 447-631 nm, 631-890 nm, 890-1256 nm, and 1256-1772 nm, respectively, in winter 2013-2014 in Xi'an.
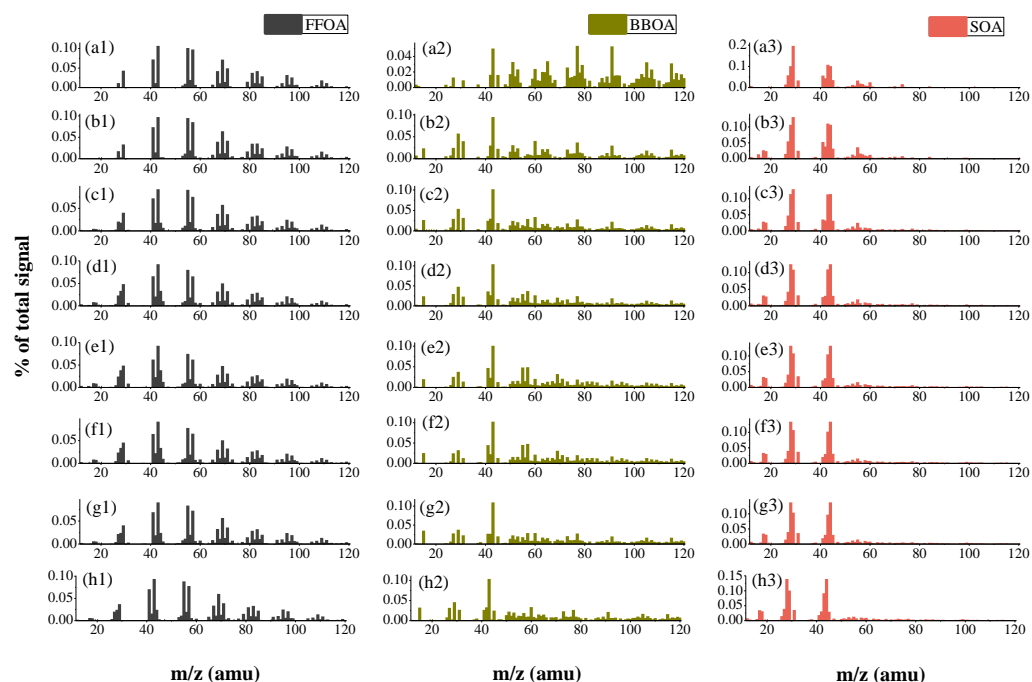
Figure ~~S2~~S3. Mass spectra of (a1-h1) FFOA, (a2-h2) BBOA, and (a3-h3) SOA under different size ranges of 112-159 nm, 159-225 nm, 225-317 nm, 317-447 nm, 447-631 nm, 631-890 nm, 890-1256 nm, and 1256-1772 nm, respectively, in winter 2018-2019 in Xi'an.
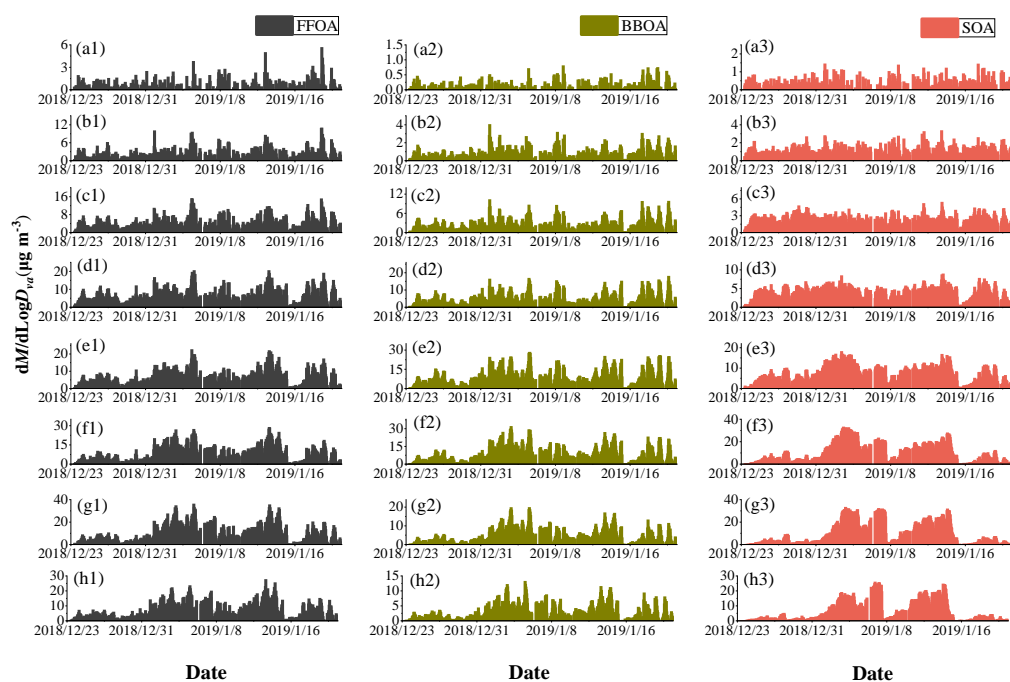
Figure S4. Time series of (a1-h1) FFOA, (a2-h2) BBOA, and (a3-h3) SOA under different size ranges of 112-159 nm, 159-225 nm, 225-317 nm, 317-447 nm, 447-631 nm, 631-890 nm, 890-1256 nm, and 1256-1772 nm, respectively, in winter 2018-2019 in Xi'an.
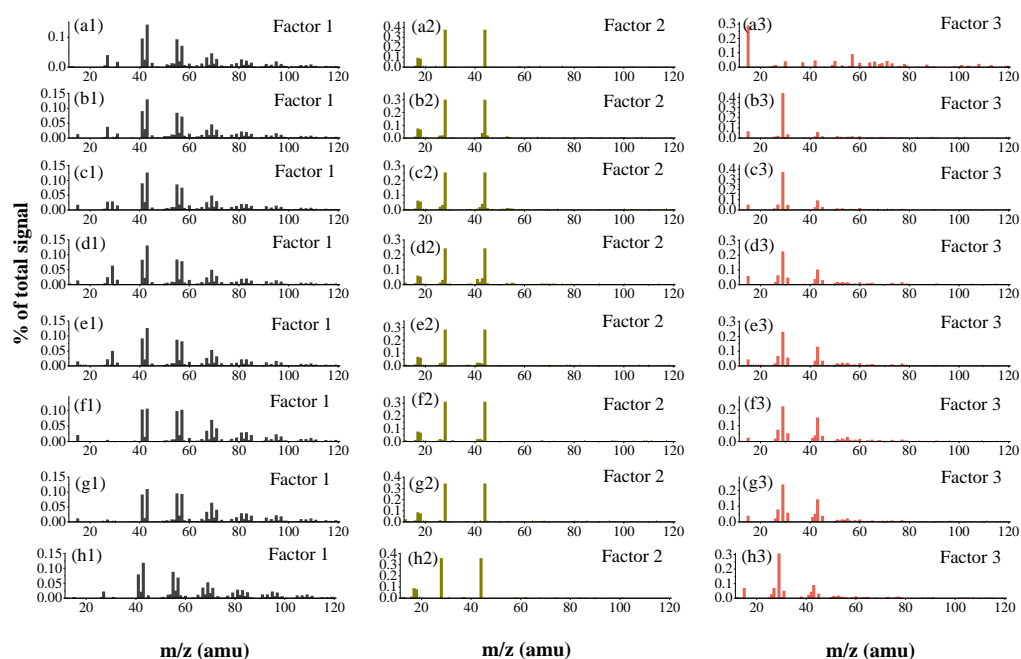
Figure S5. Mass spectra of three-factor PMF results under different size ranges of 112-159 nm, 159-225 nm, 225-317 nm, 317-447 nm, 447-631 nm, 631-890 nm, 890-1256 nm, and 1256-1772 nm, respectively, in winter 2013-2014 in Xi'an.
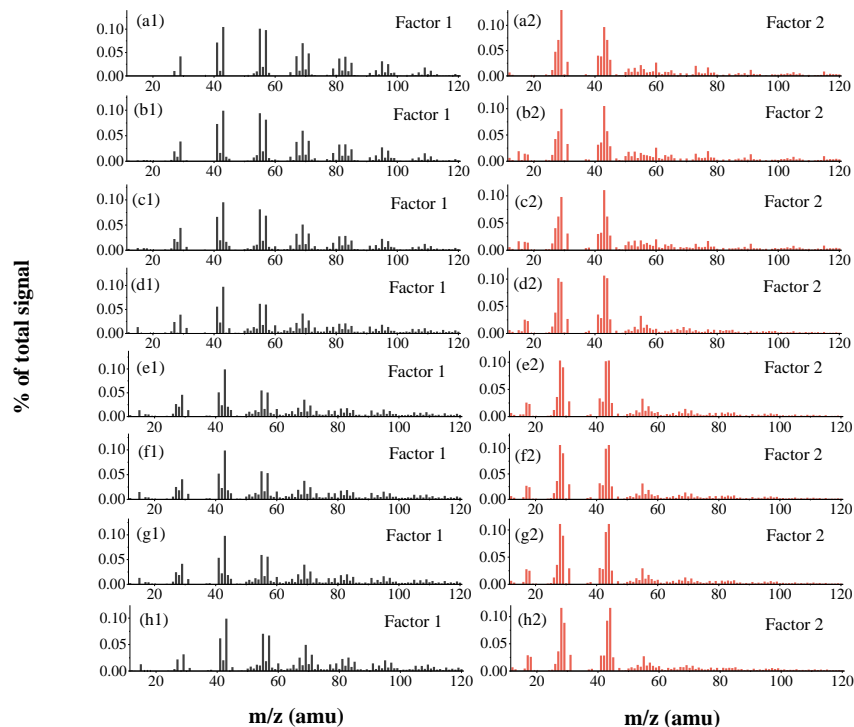
Figure S6. Mass spectra of two-factor PMF results under different size ranges of 112-159 nm, 159-225 nm, 225-317 nm, 317-447 nm, 447-631 nm, 631-890 nm, 890-1256 nm, and 1256-1772 nm, respectively, in winter 2018-2019 in Xi'an.
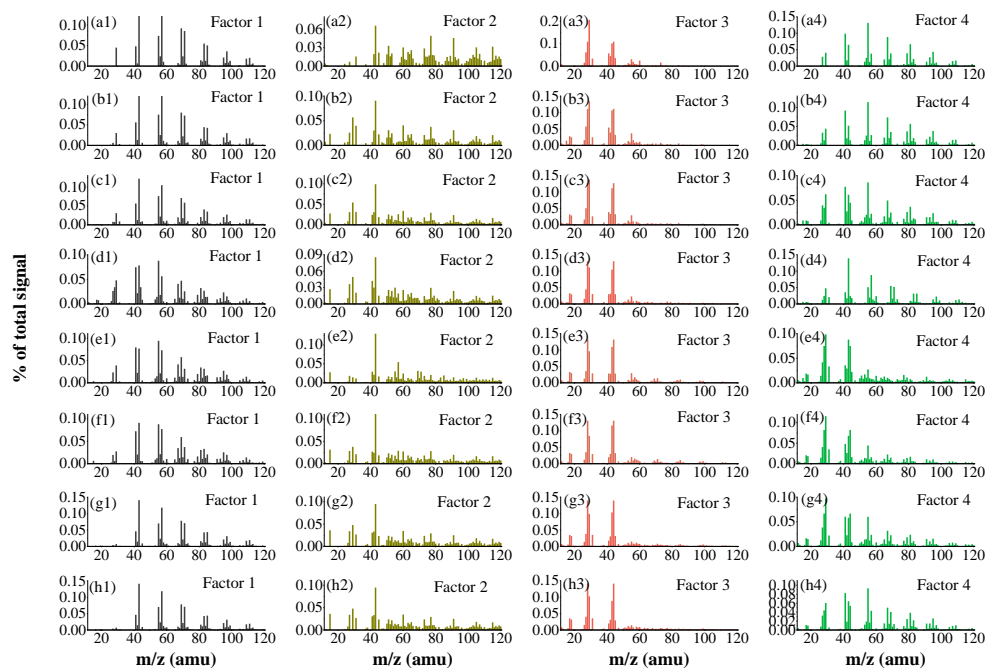
Figure S7. Mass spectra of four-factor PMF results under different size ranges of 112-159 nm, 159-225 nm, 225-317 nm, 317-447 nm, 447-631 nm, 631-890 nm, 890-1256 nm, and 1256-1772 nm, respectively, in winter 2018-2019 in Xi'an.
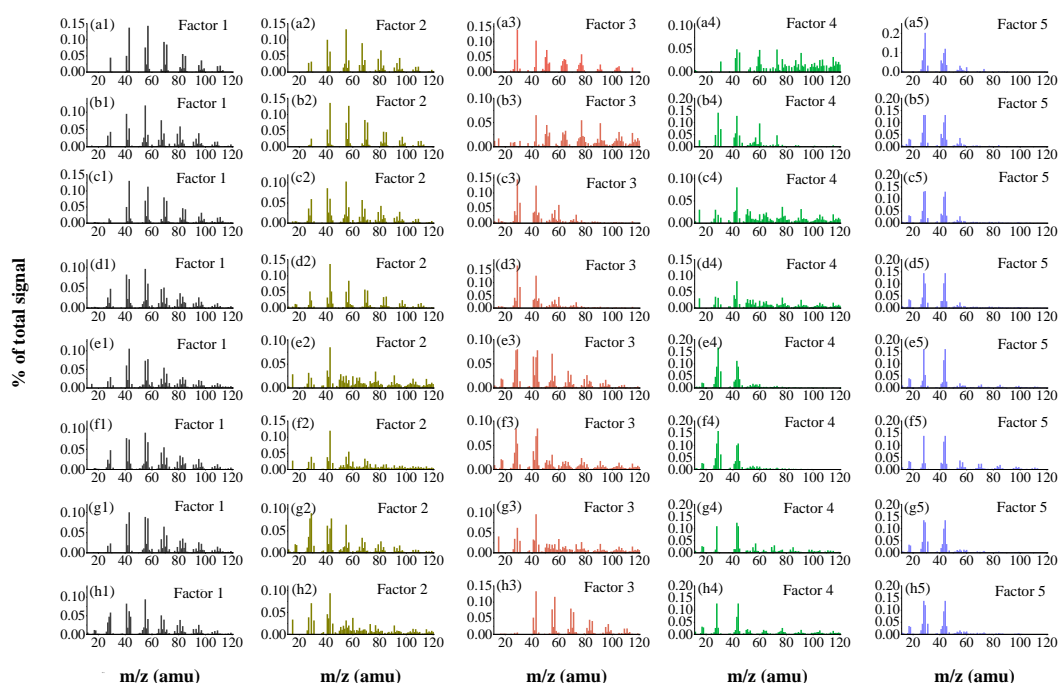
Figure S8. Mass spectra of five-factor PMF results under different size ranges of 112-159 nm, 159-225 nm, 225-317 nm, 317-447 nm, 447-631 nm, 631-890 nm, 890-1256 nm, and 1256-1772 nm, respectively, in winter 2018-2019 in Xi'an.
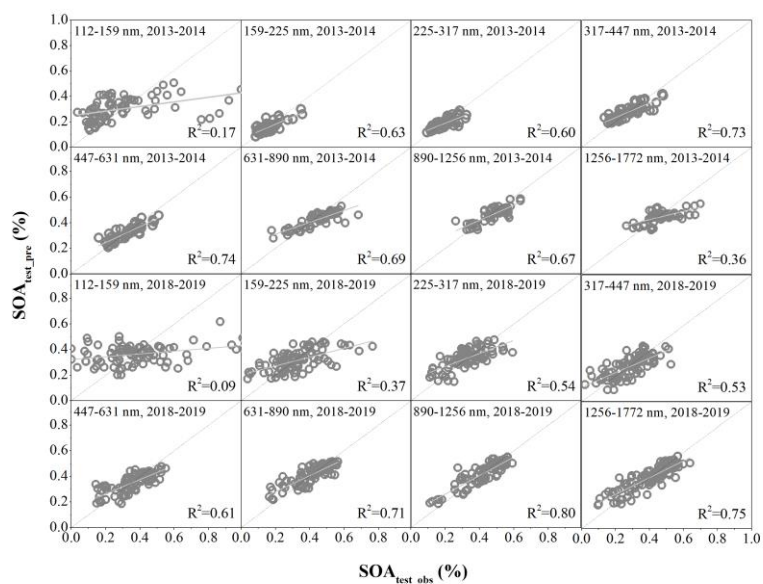
Figure S9. Correlation between the predicted and observed SOA fractions in total OA across different size ranges in the winters of 2013-2014 and 2018-2019, respectively.
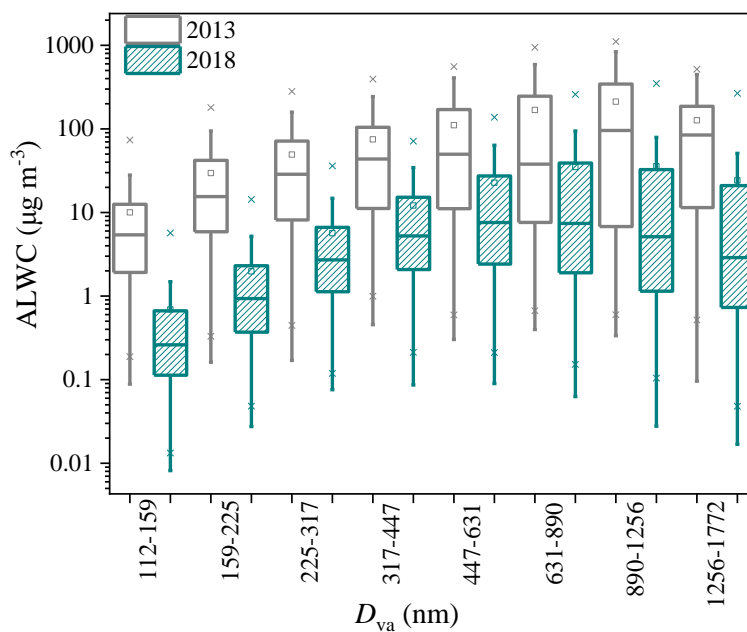
Figure ~~S3~~S10. Size distribution of ALWC between winter 2013-2014 and winter 2018-2019 in Xi'an.
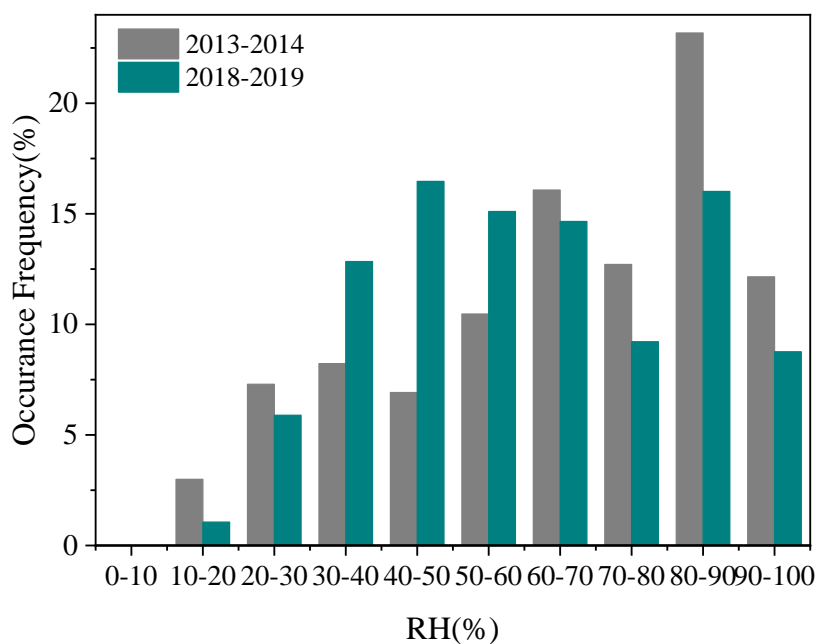
Figure ~~S4~~S11. Distribution frequency of RH between winter 2013-2014 and winter 2018-2019 in Xi'an.
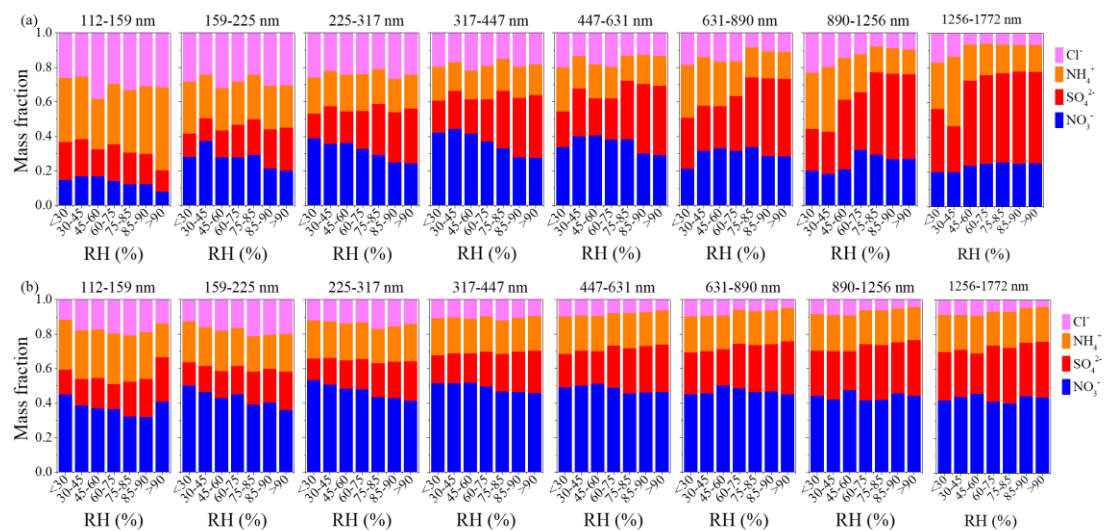
Figure ~~S5~~S12. Mass composition of inorganic species under different size ranges and RH ranges between winter 2013-2014 (a) and winter 2018-2019 (b).
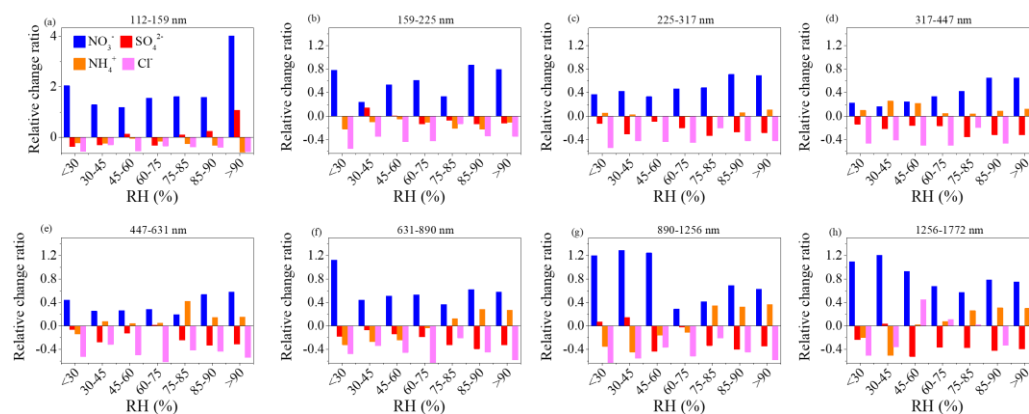
Figure ~~S6~~S13. Relative changes of mass fraction of NO₃⁻, SO₄²⁻, NH₄⁺, and Cl⁻ in total inorganic aerosol in winter 2018-2019, compared to winter 2013-2014 under different size ranges.

References:

Cubison, M. J., Ortega, A. M., Hayes, P. L., Farmer, D. K., Day, D., Lechner, M. J., Brune, W. H., Apel, E., Diskin, G. S., Fisher, J. A., Fuelberg, H. E., Hecobian, A., Knapp, D. J., Mikoviny, T., Riemer, D., Sachse, G. W., Sessions, W., Weber, R. J., Weinheimer, A. J., Wisthaler, A., and Jimenez, J. L.: Effects of aging on organic aerosol from open biomass burning smoke in aircraft and laboratory studies, Atmos. Chem. Phys., 11, 12049–12064, https://doi.org/10.5194/acp-11-12049-2011, 2011.

Hu, W. W., Hu, M., Hu, W., Jimenez, J. L., Yuan, B., Chen, W., Wang, M., Wu, Y., Chen, C., Wang, Z., Peng, J., Zeng, L., and Shao, M.: Chemical composition, sources, and aging process of submicron aerosols in Beijing: Contrast between summer and winter, J. Geophys. Res.-Atmos., 121, 1955–1977, https://doi.org/10.1002/2015JD024020, 2016.

Ng, N. L., Canagaratna, M. R., Zhang, Q., Jimenez, J. L., Tian, J., Ulbrich, I. M., Kroll, J. H., Docherty, K. S., Chhabra, P. S., Bahreini, R., Murphy, S. M., Seinfeld, J. H., Hildebrandt, L., Donahue, N. M., DeCarlo, P. F., Lanz, V. A., Prévôt, A. S. H., Dinar, E., Rudich, Y., and Worsnop, D. R.: Organic aerosol components observed in Northern Hemispheric datasets from Aerosol Mass Spectrometry, Atmos. Chem. Phys., 10, 4625–4641, https://doi.org/10.5194/acp-10-4625-2010, 2010.

Ng, N. L., Canagaratna, M. R., Jimenez, J. L., Chhabra, P. S., Seinfeld, J. H., and Worsnop, D. R.: Changes in organic aerosol composition with aging inferred from aerosol mass spectra, Atmos. Chem. Phys., 11, 6465–6474, https://doi.org/10.5194/acp-11-6465-2011, 2011.

Sun, Y. L., Du, W., Fu, P., Wang, Q., Li, J., Ge, X., Zhang, Q., Zhu, C., Ren, L., Xu, W., Zhao, J., Han, T., Worsnop, D. R., and Wang, Z.: Primary and secondary aerosols in Beijing in winter: sources, variations and processes, Atmos. Chem. Phys., 16, 8309 – 8329, https://doi.org/10.5194/acp-16-8309-2016, 2016.

Sun, Y., Xu, W., Zhang, Q., Jiang, Q., Canonaco, F., Prévôt, A. S. H., Fu, P., Li, J., Jayne, J., Worsnop, D. R., and Wang, Z.: Source apportionment of organic aerosol from 2-year highly time-resolved measurements by an aerosol chemical speciation monitor in Beijing, China, Atmos. Chem. Phys., 18, 8469–8489, https://doi.org/10.5194/acp-18-8469-2018, 2018.